Nano Research
2023, 16(5): 6805–6814

ISSN 1998-0124 CN 11-5974/O4
https://doi.org/10.1007/s12274-022-5333-z

Research Article

A double-layer covered architecture with spinel phase induced by LiPP for Co-free Li-rich cathode with high-rate performance and long lifespan

Ruiqi Zhao[1,3], Manman Wu[1,2,3], Peixin Jiao[3,4,5], Xueting Wang[1,3], Jie Zhu[1,3], Yang Zhao[1,3], Hongtao Zhang[1,3] (✉), Kai Zhang[3,4,5], Chenxi Li[1,3], Yanfeng Ma[1,3], and Yongsheng Chen[1,2,3] (✉)

[1] *The Centre of Nanoscale Science and Technology and Key Laboratory of Functional Polymer Materials, Institute of Polymer Chemistry, College of Chemistry, Nankai University, Tianjin 300071, China*
[2] *State Key Laboratory of Elemento-Organic Chemistry, Nankai University, Tianjin 300071, China*
[3] *Renewable Energy Conversion and Storage Center (RECAST), Nankai University, Tianjin 300071, China*
[4] *Department Key Laboratory of Advanced Energy Materials Chemistry (Ministry of Education), College of Chemistry, Nankai University, Tianjin 300071, China*
[5] *Engineering Research Center of High-efficiency Energy Storage (Ministry of Education), College of Chemistry, Nankai University, Tianjin 300071, China*

Received: 26 August 2022 / **Revised:** 5 November 2022 / **Accepted:** 16 November 2022

ABSTRACT

Co-free Li-rich Mn-based layered oxides are promising candidates for next-generation lithium-ion batteries (LIBs) due to their high specific capacity, high voltage, and low cost. However, their commercialization is hindered by limited cycle life and poor rate performance. Herein, an *in-situ* simple and low-cost strategy with a nanoscale double-layer architecture of lithium polyphosphate (LiPP) and spinel phase covered on top of the bulk layered phase, is developed for $Li_{1.2}Mn_{0.6}Ni_{0.2}O_2$ (LMNO) using Li^+-conductor LiPP (denoted as LMNO@S-LiPP). With such a double-layer covered architecture, the half-cell of LMNO@S-LiPP delivers an extremely high capacity of 202.5 mAh·g^{-1} at 1 A·g^{-1} and retains 85.3% of the initial capacity after 300 cycles, so far, the best high-rate electrochemical performance of all the previously reported LMNOs. The energy density of the full-cell assembled with commercial graphite reaches 620.9 Wh·kg^{-1} (based on total weight of active materials in cathode and anode). Mechanism studies indicate that the superior electrochemical performance of LMNO@S-LiPP is originated from such a nanoscale double-layer covered architecture, which accelerates Li-ion diffusion, restrains oxygen release, inhibits interfacial side reactions, and suppresses structural degradation during cycling. Moreover, this strategy is applicable for other high-energy-density cathodes, such as $LiNi_{0.8}Co_{0.1}Mn_{0.1}O_2$, $Li_{1.2}Ni_{0.13}Co_{0.13}Mn_{0.54}O_2$, and $LiCoO_2$. Hence, this work presents a simple, cost-effective, and scalable strategy for the development of high-performance cathode materials.

KEYWORDS

Co-free Li-rich layered oxides, double-layer covered architecture, lithium polyphosphate, high-rate performance, long cycle life

1 Introduction

With the rapid development of the demanded decarbonized society, the widely used lithium-ion batteries (LIBs) with high energy density are pressingly called to meet the ever-increasing requirements of commercial applications [1–4]. Therefore, possessing both a high reversible capacity of over 250 mAh·g^{-1} and a high average discharge voltage of 3.5 V for high energy density, Li-rich Mn-based layered oxides (LLOs) with a general formula of $xLi_2MnO_3{\cdot}(1-x)LiTMO_2$ (TM = Mn, Ni, Co, etc.), are considered as promising candidates for next-generation LIBs [5–7]. The extraordinary energy density of LLOs originates from the contributions of transition metal (TM) cationic and unique high-voltage oxygen anionic redox (OAR) behavior, which usually refers to the reversible O^{2-}/O_2^{n-} redox [8, 9]. Nevertheless, the oxygen atoms can be easily released after being oxidized into O_2, leading to TM migration, structural degradation, surface roughening, TM dissolution, and attenuation of correlative electrochemical performance [10, 11]. Moreover, the sluggish Li^+ diffusion in the monoclinic Li_2MnO_3 phase results in inferior diffusion kinetics and poor rate performance of LLOs [12, 13]. These fundamental challenges seriously obstruct the practical utilization of LLOs.

Numerous strategies have been pursued to address these problems, including surface coating and elemental doping [5, 14]. As oxygen loss and structural degradation tend to initiate from the particle surface, surface coating is thus an intuitive approach to addressing these issues without the risk of bulk structural damage. For instance, the utilization of various functional coatings, such as metal oxides (Al_2O_3, TiO_2, and CeO_2) [15–17] and metal fluorides (AlF_3, MgF_2, and CaF_2) [18–20], can suppress the oxygen release

Address correspondence to Hongtao Zhang, htzhang@nankai.edu.cn; Yongsheng Chen, yschen99@nankai.edu.cn

and physically separate the LLOs from electrolyte to inhibit the interfacial side reactions. However, these oxides and fluorides can hardly improve the conductivities of the cathode. Therefore, electronic conductors (carbon-based materials) and Li-ion conductors ($LiTaO_3$, Li_2TiO_3, and Li_3PO_4) have been employed to separate the cathode and electrolyte [21–24], as well as improve the electronic and Li^+ conductivities. Nevertheless, these conductive coating layers can only suppress the oxygen release physically instead of tuning oxygen redox essentially. In addition, it has been reported that the spinel/layered heterostructure constructed on the LLOs could alleviate the irreversible O_2 release by reducing the surface oxygen partial pressure, improve Li-ion diffusion by providing three-dimensional (3D) lithium diffusion channels, and suppress Jahn–Teller distortion of Mn by modulating the interfacial orbital ordering [25–30]. But this heterostructure cannot well separate the electroactive materials from the electrolyte physically to suppress the interfacial side reactions during cycling. Moreover, studies that combined the positive effects of both Li^+-conductive coatings and spinel phase layers rarely focused on Co-free LLOs (e.g., $Li_{1.2}Mn_{0.6}Ni_{0.2}O_2$ (LMNO)) cathode materials, which is in fact more proper for commercialization as a high-energy, low-cost, and environmentally friendly material [31, 32]. Therefore, it is urgent to develop a universal and economic strategy with synergistic effects by the double-layer coating for high-performance Co-free LMNO cathode.

Furthermore, the Li^+ conductivity of these LMNO materials is another limiting factor for their rate performance as mentioned above. Recently, via high-throughput computational screening, Ceder et al. proposed that the polyanionic oxides such as LiH_2PO_4, $LiTi_2(PO_4)_2$, and $LiPO_3$ are promising coating materials rendering excellent chemical stability, electrochemical stability, and outstanding Li-ion mobility [33]. Moreover, Guo et al. constructed a phospholipid-like protective layer of $AlPO_4$-Li_3PO_4 on single crystal Ni-rich cathodes, with accelerated interfacial Li^+ transport and relieved stress during cycling [34]. Hence, Li^+-conductor is believed to be a kind of ideal coating material for the layered oxides materials, including but not limited to Co-free LMNO cathode material.

Herein, with a simple and large-scalable approach, we developed a double-layer covered architecture with spinel phase induced by Li^+-conductor lithium polyphosphate (LiPP) for Co-free Li-rich cathode material LMNO (denoted as LMNO@S-LiPP). LiPP not only acts as a Li^+-conductive layer, but simultaneously induces an *in-situ* spinel phase. Accordingly, the nanoscale double-layer covered architecture effectively promotes the Li-ion diffusion rate, restrains the oxygen release, and inhibits the interfacial side reactions, so that it suppresses the structural degradation, mitigates TM dissolution as well as restrains the voltage decay during charge/discharge. Consequently, this double-layer structure endows LMNO@S-LiPP cathode with superior electrochemical performance. The LMNO@S-LiPP half-cell delivers a high capacity of 202.5 $mAh·g^{-1}$ at 1 $A·g^{-1}$ and a high capacity retention of 85.3% after 300 cycles, outperforming the previously reported LMNO-based cathodes. Besides, the LMNO@S-LiPP||graphite full-cell renders an energy density of 620.9 $Wh·kg^{-1}$ (based on total weight of active materials in cathode and anode). Furthermore, this strategy exhibits a good generalization and could be applied for other similar layered oxides materials with significant enhanced performance.

2 Results and discussion

2.1 Synthesis and characterization

The pristine LMNO was prepared through a typical co-precipitation technique followed by solvothermal as well as the solid-state reaction method. To prepare LMNO@S-LiPP, the pristine LMNO was added into the methanol solution of LiOH, followed by the addition of polyphosphoric acid (PPA) in methanol solution, as illustrated in Scheme 1 (details in the Electronic Supplementary Material (ESM)) [35, 36]. Therefore, the LMNO@S-LiPP was obtained by covering the *in-situ* formed LiPP which was originated from the reaction of LiOH and PPA. The structures of pristine LMNO and LMNO@S-LiPP were first verified by the powder X-ray diffraction (p-XRD) and corresponding Rietveld refinement, as shown in Fig. S1 in the ESM and Fig. 1(a). Both patterns reveal the characteristic diffraction peaks of the well-crystallized α-$NaFeO_2$ structure with $R\bar{3}m$ space group and a monoclinic Li_2MnO_3-like structure with $C2/m$ space group. Specifically, the evident splits of (006)/(102) and (018)/(110) are observed, suggesting the well-ordered layered structure [37]. Meanwhile, a few broad superlattice reflections in the 2θ range of 20° to 25° are caused by the short-range ordering of Li/Mn cations in the TM layer, indicating the presence of Li_2MnO_3 [38]. The unit cell parameters calculated by the General Structure Analysis System (GSAS) are listed in Tables S1 in the ESM, which are convincing with R_{wp} < 2%. The patterns fit well with the experimental results. The p-XRD patterns and the refined crystallographic parameters demonstrate that the bulk structure of LMNO@S-LiPP is well maintained after LiPP covering [39, 40]. The chemical compositions of LMNO and LMNO@S-LiPP were

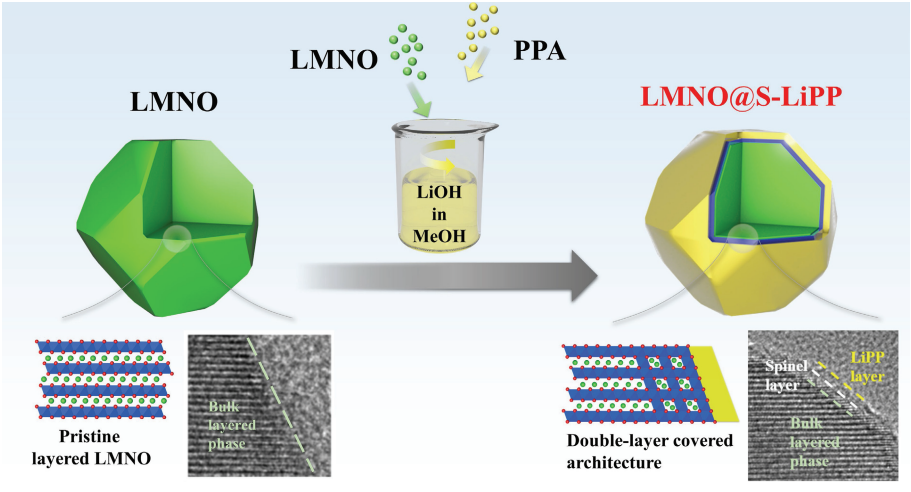

Scheme 1 Schematic diagram of the *in-situ* preparation process of double-layer covered architecture of LMNO@S-LiPP induced by LiPP.

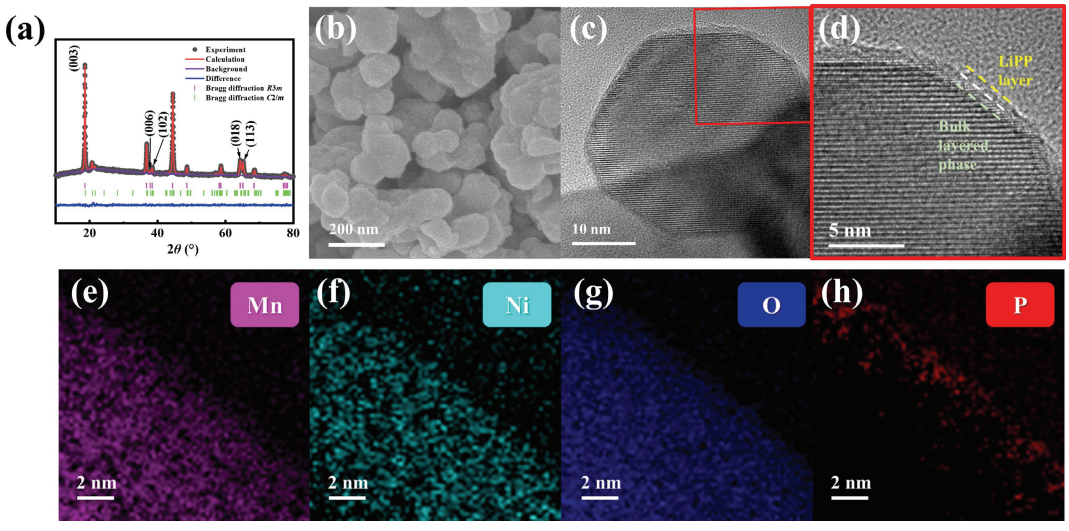

Figure 1 (a) Rietveld refinement of the p-XRD pattern of LMNO@S-LiPP. (b) FESEM image of LMNO@S-LiPP. (c) HRTEM image of LMNO@S-LiPP. (d) Magnified image of the red region in (c). EELS maps of (e) Mn, (f) Ni, (j) O, and (h) P of LMNO@S-LiPP.

confirmed by inductive coupled plasma optical emission spectrometry (ICP-OES) results, as presented in Table S2 in the ESM. The morphologies of LMNO and LMNO@S-LiPP were characterized by field emission scanning electron microscopy (FESEM) (Fig. S2(a) in the ESM and Fig. 1(b)). Both materials are composed of the small irregular polyhedral primary particles with average diameters of ~ 100 nm. Moreover, the distributions of chemical elements in LMNO and LMNO@S-LiPP were confirmed by the energy-dispersive X-ray spectroscopy (EDS), as displayed in Figs. S3 and S4 in the ESM. It is presented that the main elements including Mn, Ni, and O in LMNO and Mn, Ni, O, and P in LMNO@S-LiPP are uniformly distributed in the samples, respectively. Meanwhile, the phosphorus existence was also confirmed by the X-ray photoelectron spectroscopy (XPS), as exhibited in Fig. S5 in the ESM. The XPS spectrum of LMNO@S-LiPP shows an extra peak of 133.8 eV compared to the pristine LMNO, which corresponds to the presence of phosphorus on the surface of LMNO@S-LiPP. Furthermore, high-resolution transmission electron microscopy (HRTEM) was carried out to illustrate the successful surface coating of LiPP, as exhibited in Figs. 1(c) and 1(d). A nanoscale LiPP layer can be clearly recognized between the yellow-white dashed line, beside which a thin layer with structural transformation can be observed between the white-green dashed line, while the layered structure is well maintained in the bulk. To evidence the nanoscale phosphorus-based LiPP layer, electron energy loss spectroscopy (EELS) was also performed on the surface of LMNO@S-LiPP. The EELS mapping analysis reveals a distinct phosphorus layer on the particle surface (Figs. 1(e)–1(h) and Fig. S6 in the ESM). These above results suggest that a uniform LiPP envelop is successfully introduced around the LMNO particle without bulk structural damage.

To further investigate the detailed surface structure at the atomic scale, the LMNO@S-LiPP particle was observed by the high-angle annular dark-field scanning transmission electron microscopy (HAADF-STEM). As observed in Fig. 2(a), in the bulk region, LMNO@S-LiPP displays a layered phase structure with an interplanar spacing of 0.471 nm, which is typically indexed to the (003) plane when the viewing direction is [010] zone axis [29, 41]. On the top of the bulk layered LMNO, a few atomic layers of ordered spinel structure are sandwiched between the top amorphous LiPP layer and the bulk layered phase (labeled between the yellow-white dashed line in Fig. 1(d)). The nanometer's thickness spinel phase is well recognized along with the [110] zone axis with an interplanar distance of 0.236 nm,

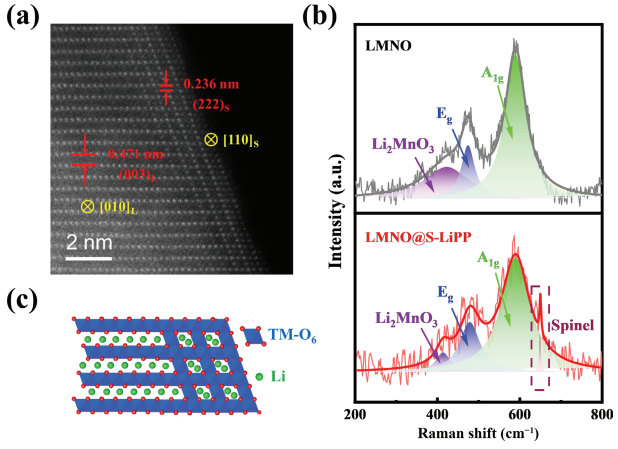

Figure 2 (a) HAADF-STEM image of LMNO@S-LiPP particle. (b) Raman spectra of the pristine LMNO and LMNO@S-LiPP. (c) Corresponding crystallographic model of atomic arrangement in LMNO@S-LiPP particle.

which is corresponding to the (222) planes [29, 41]. This surface structure is shown schematically in Fig. 2(c). Besides, Raman scattering is also commonly used to distinguish the structural difference between layered and spinel phases from the TM–O bonds, which was applied for the pristine LMNO and LMNO@S-LiPP materials [35, 42–44]. The Raman spectrum of the pristine LMNO contains a weak peak at about 415 cm^{-1}, which is attributed to the A_g mode of monoclinic Li_2MnO_3, while the peaks at 480 and 590 cm^{-1} belong to the A_{1g} (O–TM–O) stretching vibrations and E_g (TM–O) bending vibrations of $R\bar{3}m$ layered structure, respectively (Fig. 2(b)) [25, 45, 46]. Compared with the pristine LMNO, there is an extra shoulder peak at 630 cm^{-1}, which is related to the Mn–O vibrations of the spinel phase in the LMNO@S-LiPP spectrum, validating the existence of the *in-situ* formed spinel phase after processed by LiPP [43, 47]. Thus, the designed nanoscale double-layer covered architecture has been successfully constructed on the LMNO@S-LiPP surface by one-step *in-situ* coating of LiPP.

2.2 Electrochemical performance

We first studied electrochemical performance using coin-type half-cells within the potential window of 2.0–4.8 V (vs. Li/Li^+). In the cyclic voltammogram (CV) curve of LMNO@S-LiPP (Fig. S7 in the ESM), an oxidation peak emerged near 3.02 V (vs. Li/Li^+) compared to the pristine LMNO, which could be attributed to the spinel phase surface layer induced by the top LiPP coating layer,

according with the HAADF-STEM results [48, 49]. Figure 3(a) presents the initial galvanostatic charge/discharge profiles at 0.1 C (1 C = 200 mA·g^{-1}, following the reported literature) [48, 50–52]. Specifically, the pristine LMNO electrode exhibits the first discharge capacity of 272 mAh·g^{-1} with an initial coulombic efficiency (ICE) of 82%, while the LMNO@S-LiPP electrode delivers an initial capacity of 299.6 mAh·g^{-1} with an improved ICE of 86.4%. With the double-layer covered architecture, LMNO@S-LiPP manifests an extraordinary rate performance (Fig. 3(b)), which displays a high specific capacity of 236.5, 219.2, 202.9, 192.0, and 182.0 mAh·g^{-1} at 1, 2.5, 5, 7.5, and even 10 C, respectively, whereas the corresponding capacity of the pristine LMNO is found to be 192.6, 167.4, 140.7, 130.2, and 113.7 mAh·g^{-1} (see Fig. S8 in the ESM for the corresponding capacity–voltage profiles under selected current densities). As mentioned earlier, the Co-free Li-rich cathodes suffer from severe voltage decay, which greatly decreases the energy density and impedes practical applications. Figure 3(c) shows that the LMNO@S-LiPP electrode exhibits a better voltage stability with an average discharge voltage of 3.01 V after 300 cycles at 1 C, which is 0.63 V higher than that of the pristine LMNO electrode. During 300 cycles, LMNO@S-LiPP has a mitigated voltage decay rate of only 1.31 mV per cycle, which is significantly smaller than that of 3.25 mV per cycle for the pristine LMNO. The inhibited voltage decay originates from the better structure stability as discussed below, which also improves the prolonged cycling performance (Figs. 3(d) and 3(e)). LMNO@S-LiPP demonstrates a discharge capacity of 205.3 mAh·g^{-1} with a capacity retention of 84.0% after 200 cycles under 1 C, and still remains 70.0% after 300 cycles. Moreover, under the harsher condition cycling at 5 C, LMNO@S-LiPP retains 90.5% (183.5 mAh·g^{-1}) of the initial capacity after 200 cycles. Even after 300 cycles, LMNO@S-LiPP still delivers a capacity of 172.2 mAh·g^{-1} with the capacity retention of 85.3%. These results indicate that with the double-layer covered architecture, the high-rate electrochemical performance of LMNO@S-LiPP is among the best of all the reported LMNO-based cathode materials (Table 1) [31, 32, 48, 50–55]. By comparison, the discharge capacity of pristine LMNO decreases rapidly and it retains only 53.7% (112.3 mAh·g^{-1}) of the initial capacity under 1 C after 200 cycles. The discharge capacity of the pristine LMNO under 5 C rapidly falls to 70.8 mAh·g^{-1} after 200 cycles with the retention of 54%. The charge–discharge voltage profiles of both cathodes at 1 C and 5 C during 1st, 50th, 100th, …, 300th cycles are exhibited in Fig. S9 in the ESM. It shows that LMNO@S-LiPP cathode has smaller gaps than LMNO between charge and discharge curves, indicating the reduced polarization of LMNO@S-LiPP during cycling due to the existence of double-layer architecture in this material [56].

More importantly, a coin-type full-cell with LMNO@S-LiPP cathode paired with commercial graphite anode was assembled to evaluate its real performance in practical scenario. As depicted in Fig. S10 in the ESM, the LMNO@S-LiPP delivers a specific discharge capacity of 280.2 mAh·g^{-1} in the LMNO@S-LiPP||graphite full-cell, and the full-cell demonstrates a high energy density of 620.9 Wh·kg^{-1} based on all the active materials. Besides, after 100 cycles at 1 C, the full-cell exhibits excellent capacity retention of 90.2%. Moreover, the LMNO@S-LiPP||graphite pouch cell was also constructed, which is presented in Fig. S11(a) in the ESM. This pouch cell retains 74.5% of the initial discharge capacity and 68.3% of the initial energy density after 100 cycles (Fig. S11(b) in the ESM). These results indicate that this Co-free Li-rich material with the designed double-layered

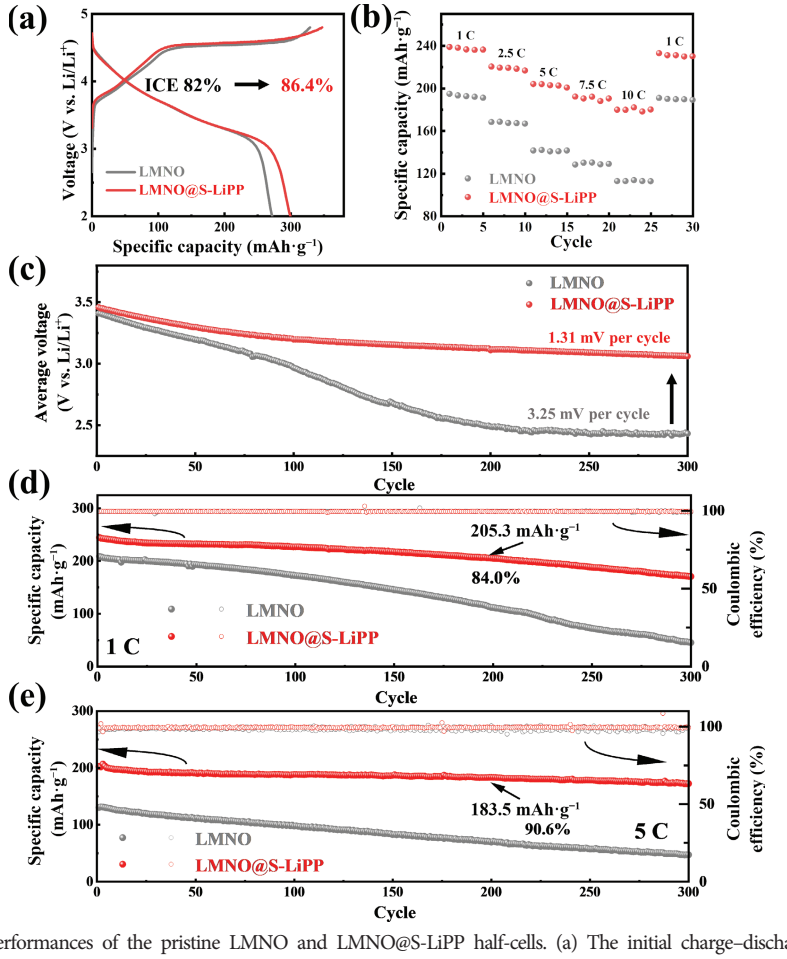

Figure 3 The electrochemical performances of the pristine LMNO and LMNO@S-LiPP half-cells. (a) The initial charge–discharge profiles at 0.1 C. (b) Rate performances under different current densities. (c) The average operating voltage during discharge at 1 C. Cycling performances at (d) 1 C and (e) 5 C.

Table 1 Capacities under 0.1 C, 1 C, and 5 C of LMNO@S-LiPP and related literatures of $Li_{1.2}Mn_{0.6}Ni_{0.2}O_2$-based materials

	0.1 C capacity ($mAh·g^{-1}$)	1 C capacity ($mAh·g^{-1}$)	1 C capacity (100 cycles) ($mAh·g^{-1}$)	5 C initial capacity ($mAh·g^{-1}$)	5 C capacity (200 cycles) ($mAh·g^{-1}$)	Ref.
1	—	196	194	—	—	[51]
2[a]	~ 250	188.0	188.0	125.0	125.8	[32]
3	259.1	204.6	195.6	135.7	—	[53]
4	291.8	~ 230	196.8	~ 215	170.3 (100 cycles)	[55]
5	296.6	~ 230	~ 230	~ 198	—	[48]
6	~ 294	~ 225	—	138.5	129.2 (300 cycles)	[54]
7[a]	~ 237	~ 175	—	~ 135	~ 135	[50]
8	~ 253	~ 197	~ 176	149.4	~ 138	[31]
9	**299.6**	**244.5**	**226.9**	**202.5**	**183.5**	**This work**

[a]In this work 1 C = 250 $mAh·g^{-1}$.

structure of LiPP and spinel phase on top of the bulk layered phase indeed exhibits great potential for next-generation high-energy LIBs.

2.3 Kinetics and mechanism studies

Considering the outstanding rate performance of LMNO@S-LiPP, further study was conducted on the kinetics of the half-cells of pristine LMNO and LMNO@S-LiPP. As a reliable method, galvanostatic intermittent titration technique (GITT) was employed to quantify the Li^+ diffusion coefficient (D_{Li^+}) [57–59]. We performed GITT measurements of electrodes at the current density of 0.1 C with 30 min discharge and 1.5 h relaxation for each step. Figure 4(a) shows GITT curves of the discharge process for the pristine LMNO and LMNO@S-LiPP. The overpotential values of LMNO@S-LiPP are apparently smaller than those of the pristine LMNO, suggesting that LMNO@S-LiPP possesses better Li^+ diffusion kinetics than the pristine LMNO. To further quantify this elevation, D_{Li^+} values are calculated according to the equation in Note S1 in the ESM following the standard protocol method and those values of LMNO and LMNO@S-LiPP are compared in Fig. 4(b) [60]. It is demonstrated that the D_{Li^+} values of LMNO@S-LiPP are one-order higher than those of the pristine LMNO at each discharge voltage. These results illustrate that the surface reconstruction by double-layer covered with spinel phase layer and LiPP plays an important role in improving the Li-ion diffusion kinetics of LMNO material, as both LiPP layer and induced spinel phase on the particle surface possess high Li-ion conductivity. To further evaluate the influence of this double-layer covered architecture on the internal impedance, electrochemical impedance spectroscopy (EIS) was performed before and after cycling. Figure 4(c) displays the experimental Nyquist plots, consisting of semicircles in the intermediate-frequency region and oblique lines in the low-frequency region [36]. The Nyquist plots were well fitted with a simplified equivalent circuit model as shown in Fig. S12 in the ESM, and the results are exhibited in Fig. 4(f). The charge transfer and interfacial film resistance are represented by R_{ct} and R_f, respectively. Compared with the pristine LMNO, both R_{ct} and R_f of the LMNO@S-LiPP are significantly lower. Especially after cycling, the resistance values of the LMNO@S-LiPP are as low as one-tenth the values of the pristine LMNO, which is attributed to the fast reaction kinetics, stable surface structure, and suppressed interfacial side reactions of LMNO@S-LiPP [61]. Hence, a significantly improved high-rate capability for LMNO@S-LiPP can be achieved, which is in accordance with the above-mentioned electrochemical performance.

To understand the mechanism of the decreased R_f, XPS was conducted to study the chemical composition of the cathode electrolyte interface (CEI) of the pristine LMNO and LMNO@S-LiPP electrodes after cycling. In the high-resolution O 1s spectrum in Fig. 4(d), the peak at ~ 529.6 eV is assigned to the transition metal oxide (TM–O) in the cathode material, while the peaks at ~ 531.9 and ~ 533.1 eV are attributed to the C=O and O–C=O respectively, representing the decomposition products of the electrolyte solvent from the interfacial side reactions [62]. In comparison, the intensity of the TM–O peak in LMNO@S-LiPP is significantly stronger than that of the pristine LMNO, while the intensities of C=O and O–C=O peaks are lower, which indicates the less decomposition product on the surface of LMNO@S-LiPP cathode. Meanwhile, in the C 1s spectrum (Fig. S13(a) in the ESM), the peak at ~ 284.8 eV can be attributed to the C–C of the conductive carbon in the cathode. The peaks at ~ 286.0, ~ 289.1, and ~ 290.1 eV correspond to C–O, O–C=O, and $ROCO_2Li$, respectively [57]. These peaks resulted from the electrolyte decomposition in LMNO@S-LiPP are lower than those in LMNO as well, which is consistent with O 1s spectrum. Besides, in the high-resolution P 2p spectrum in Fig. 4(e), the peak at ~ 136.5 eV corresponds to Li_xPF_y, while the peak at ~ 133.9 eV belongs to $Li_xPO_yF_z$ and LiPP, whereas Li_xPF_y and $Li_xPO_yF_z$ are the decomposition products of $LiPF_6$ due to the interfacial side reactions [24, 63–65]. Similarly, the Li_xPF_y peak intensity in the CEI of LMNO@S-LiPP is relatively lower than that of the pristine LMNO. As for the high-resolution F 1s spectrum (Fig. S13(b) in the ESM), the peak at around ~ 688.1 eV (C–F) can be assigned to the polyvinylidene fluoride (PVDF) binder. The peak corresponding to Li–F at ~ 685.0 eV is mainly attributed to the decomposition of $LiPF_6$ from the electrolyte. The intensity of Li–F in LMNO@S-LiPP is significantly lower than that in LMNO, which indicates the suppressed decomposition of $LiPF_6$ [66]. These results reveal that the deposition of side reaction products is successfully suppressed by the double-layer structure covering. Moreover, the results of time-of-flight secondary ion mass spectrometry (ToF-SIMS) measurements are consistent with the XPS results, which illustrate the 3D spatial distribution of the characteristic ions in CEI layers on the cathode. The fragment ions LiF_2^- and $PO_2F_2^-$ are generated due to the hydrolysis of $LiPF_6$, which deposit a thinner layer on the surface of LMNO@S-LiPP cathode than that on the pristine LMNO as depicted in Fig. S14 in the ESM [67–69]. This indicates that the double-layer covered architecture effectively inhibits the deposition of the side reaction products by isolating the electrode from electrolyte. Therefore, the designed double-layered structure reduces the interfacial side reactions, forms a thinner CEI, lowers R_f, and improves the electrochemical performance of LMNO@S-LiPP.

In order to have a better understanding of the voltage and capacity attenuation, *operando* differential electrochemical mass

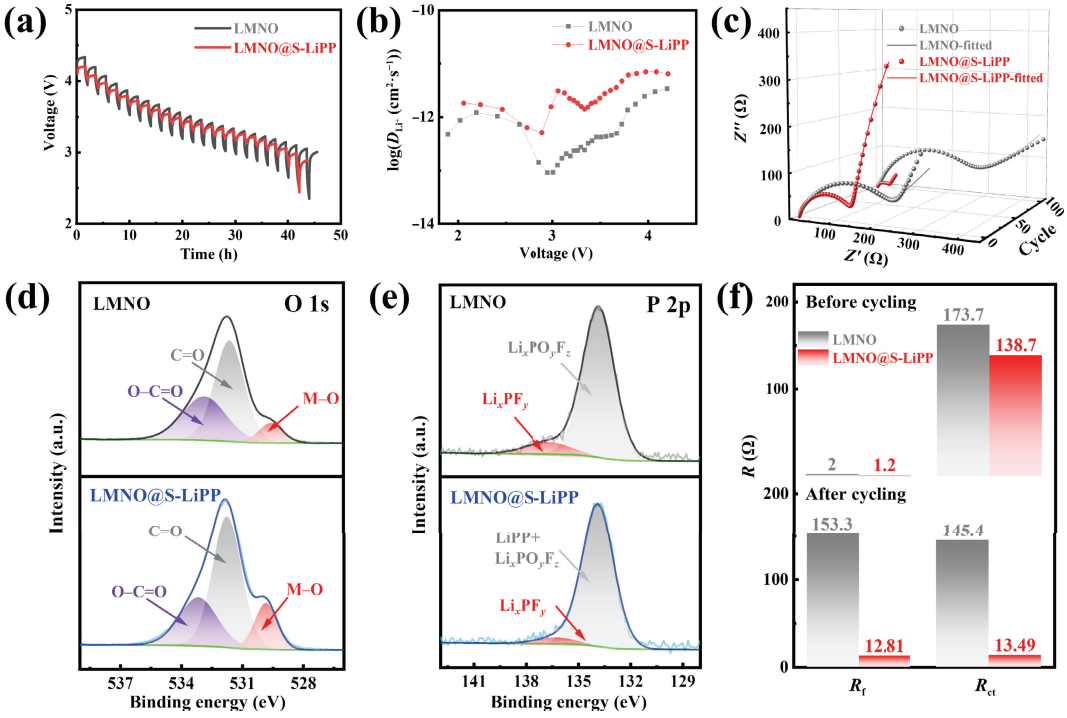

Figure 4 (a) The potential response curves from GITT measurements during discharge in the 2nd cycle. (b) The calculated Li^+ diffusion coefficient from GITT results. (c) Nyquist plots before and after cycling. High-resolution XPS spectra of (d) O 1s and (e) P 2p after 100 cycles at 1 C. (f) R_{ct} and R_f values before and after cycling.

spectrometry (DEMS) and differential capacity versus voltage (dQ/dV) were carried out for both the pristine LMNO and LMNO@S-LiPP cathodes. It is believed that the oxygen release would lead to continuous structural degradation [10]. DEMS measurements were conducted to monitor O_2 gas evolution of both cathodes during the initial cycle. Figure S15 in the ESM shows that within the voltage range of 4.5–4.8 V (vs. Li/Li^+), the O_2 evolution peak of LMNO@S-LiPP is evidently mitigated compared with the pristine LMNO. The cumulative O_2 detected from LMNO@S-LiPP is reduced to nearly half of that from the pristine LMNO. It suggests that the irreversible O_2 release of LMNO@S-LiPP is effectively ameliorated, which is in agreement with the higher initial discharge capacity and higher ICE of LMNO@S-LiPP cathode. Hence, the double-layer structure on top of the bulk can improve reversibility of anion redox and structural stability for the reversible Li^+ (de)intercalation, to further restrain the TM migration and structural degradation during the initial cycle.

The evolution of phase transition and voltage variation during Li^+ (de)intercalation were more directly monitored by differential capacity versus voltage (dQ/dV) curves, whose peak locations and intensities during the 100 cycles of both cathodes are depicted in Figs. 5(a) and 5(b). The redox pair at about 3.0 V originates from the $Mn^{4+/3+}$ redox in spinel and layered structure, and the other at about 4.0 V arises from the redox of $Ni^{4+/2+}$ [48, 70–72]. During cycling, the redox peak positions of LMNO@S-LiPP remain unchanged as marked in the red-dotted boxes in Figs. 5(a) and 5(b), which indicates the sustained electrochemical reactions of the $Mn^{4+/3+}$ redox in the LMNO@S-LiPP cathodes without change. Meanwhile, these peak intensities exhibit only slight decreases at high voltage, indicating the good structural stability throughout the cycling process [73]. By comparison, during charge in Fig. 5(a), the oxidation peaks of the pristine LMNO move towards a higher potential obviously, while during discharge in Fig. 5(b), the reduction peaks of the pristine LMNO dramatically shift to a lower potential. These results indicate the aggravation of voltage hysteresis in the pristine LMNO, which is due to the exacerbated polarization, interfacial side reactions, and structural degradation [70]. Moreover, the peak intensities of the pristine LMNO marked in the grey-dotted box constantly decrease both during charge and discharge. After cycling, the reduction peak position of $Mn^{4+/3+}$ in the pristine LMNO is completely moved to the electrochemical-inactivated disordered rocksalt region due to the severe phase transition [74]. Therefore, the designed double-layer covered architecture with LiPP and spinel phase effectively mitigates the structural degradation and phase transition during cycling.

The suppression of structural decay has also been confirmed by the HRTEM images. As presented in Fig. 5(c), the bulk region of LMNO@S-LiPP still preserved most of the original layered structure, and only 5 nm thickness spinel phase layer is generated on the bulk surface of LMNO@S-LiPP. No electrochemical-inactivated disordered rocksalt region is observed. By contrast, in Fig. 5(d), a considerable amount of spinel and rocksalt regions randomly distribute in the bulk of pristine LMNO after cycling, indicating the occurrence of uncontrollable severe structural conversion during cycling [75]. Furthermore, along with the structural degradation, LMNO also suffers from the issue of severe TM dissolution. Thus, we examined the TM (Mn and Ni) ions concentrations in electrolytes after 200 cycles at 1 C by ICP-OES. As shown in Fig. S16 in the ESM, compared to LMNO, the concentrations of dissolved Mn and Ni in the electrolyte from LMNO@S-LiPP are significantly reduced from 658 to 129 μg·mL^{-1} and from 168 to 30 μg·mL^{-1}, respectively. This result directly shows that TM dissolution in LMNO@S-LiPP can be prominently alleviated. Therefore, owing to the synergistic effect of the double-layer structure of LiPP and spinel phase, LMNO@S-LiPP maintains a high capacity after cycling, along with a relatively high average discharge voltage.

Based on the results and analysis above, Scheme 2 illustrates the synergistic effect on LMNO@S-LiPP cathode material during cycling by the double-layer covered architecture. Initially, a spinel phase layer is *in-situ* formed and sandwiched between the top LiPP layer and the bulk layered phase. The double-layer structure of LMNO@S-LiPP is able to accelerate the Li-ion diffusion because of its high Li-ion conductivity. Moreover, it reduces the irreversible capacity by mitigating the oxygen release as well as

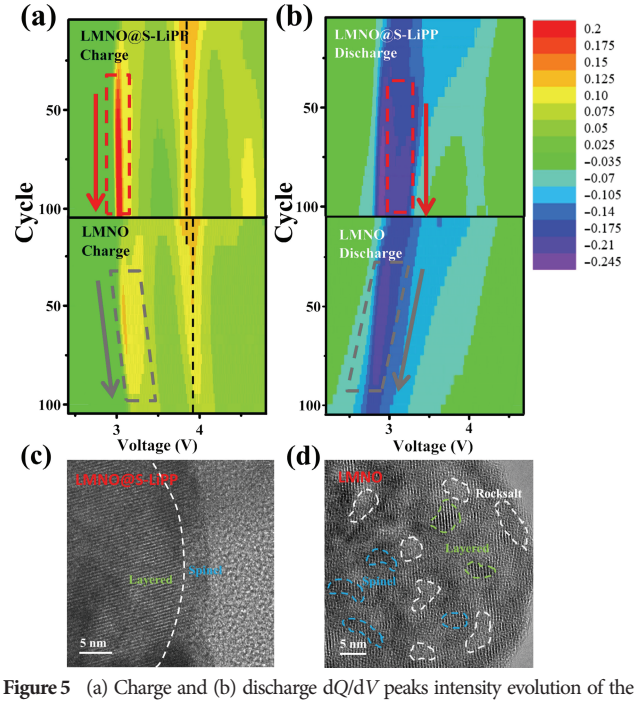

Figure 5 (a) Charge and (b) discharge dQ/dV peaks intensity evolution of the pristine LMNO and LMNO@S-LiPP cathodes during cycling at 1 C from 1st, 5th, …, 100th cycles. HRTEM images of (c) pristine LMNO and (d) LMNO@S-LiPP particles after 100 cycles at 1 C.

suppresses the cathode–electrolyte interfacial side reactions during cycling, resulting in a thin CEI with a lower R_f and better kinetics. Besides, the structural failure is also ameliorated, as evidenced by the dQ/dV curves and HRTEM images. However, the pristine LMNO material degrades rapidly due to the interfacial side reactions and by-product deposition. Hence, the proposed double-layer covered architecture of our designed LMNO@S-LiPP is highly promising for the development of high-performance cathode material.

2.4 Strategy generalization

More importantly, a generalized surface engineering is required for the commercialization of cathode materials. Thus, the LiPP covering strategy was extended to other attractive layered cathode materials, including $LiNi_{0.8}Co_{0.1}Mn_{0.1}O_2$ (NCM811), $Li_{1.2}Mn_{0.54}Co_{0.13}Ni_{0.13}O_2$ (LMCNO), and $LiCoO_2$ (LCO). The half-cells of NCM811, LMCNO, and LCO were tested within the potential windows of 2.5–4.3, 2.0–4.8, and 2.8–4.3 V (vs. Li/Li^+), respectively. As shown in Fig. S17(a) in the ESM, the ICE of NCM811 coated by LiPP (NCM811@LiPP) increases by 3%, which can be attributed to the separation of NCM811 and electrolyte by LiPP coating layer. Consequently, the initial discharge capacity of NCM811@LiPP is improved to 211.9 mAh·g^{-1} (Fig. 6(a)). With the suppressed interfacial side reactions, the NCM811@LiPP cathode renders an extra capacity of 35.6 mAh·g^{-1} compared with the bare NCM811 after 150 cycles under 0.5 C (Fig. S17(c) in the ESM) with a capacity retention of 80.0% (red stars in Fig. 6(b)). Meanwhile, the high-rate performance of NCM811@LiPP under the current density at 5 C is also promoted to a quite high level as 172.1 mAh·g^{-1} (Fig. 6(c)). Analogously, as exhibited in Fig. 6 and Figs. S17(d)–S17(j) in the ESM, LiPP coating also endows the LMCNO and LCO with high ICE, excellent cycling performance, and superior rate performance. The initial discharge capacity of LMCNO coated by LiPP (LMCNO@LiPP) exhibits as high as 306.0 mAh·g^{-1} at 0.1 C and 245.3 mAh·g^{-1} at 1 C with 28.8 mAh·g^{-1} higher than the pristine LMCNO. In the meantime, the LiPP-coated LCO (LCO@LiPP) presents a high-rate performance of 133.0 mAh·g^{-1} at 5 C, which is 17.8 mAh·g^{-1} higher than pristine LCO. The overall improved electrochemical performances of cathode materials in this work are summarized in the Table 2 and Fig. 6(d). These results indicate that our surface engineering of LiPP covering is promising to be applied in large-scale energy storage systems with broader applicability, lower cost, simpler preparation, and better electrochemical performance.

3 Conclusions

In summary, we have developed a simple and cost-effective double-layer covering strategy towards the high electrochemical performance Co-free Li-rich cathode, which introduced an *in-situ* formed spinel phase sandwiched between the top LiPP layer and the bulk layered structure. The detailed kinetics and mechanism studies of LMNO@S-LiPP and pristine LMNO reveal that this double-layer covered architecture effectively facilitates the redox reaction kinetics, inhibits the oxygen release, suppresses interfacial side reactions, and mitigates the severe phase transformations. Therefore, the LMNO@S-LiPP cathodes exhibit extraordinarily

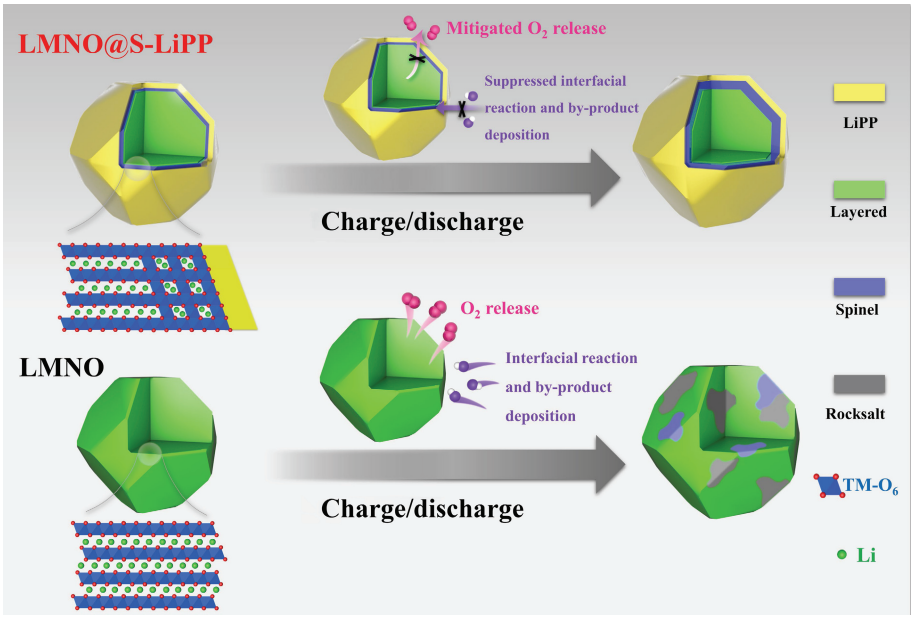

Scheme 2 Schematic illustration of the impact of the double-layer architecture on Co-free Li-rich cathodes during cycling.

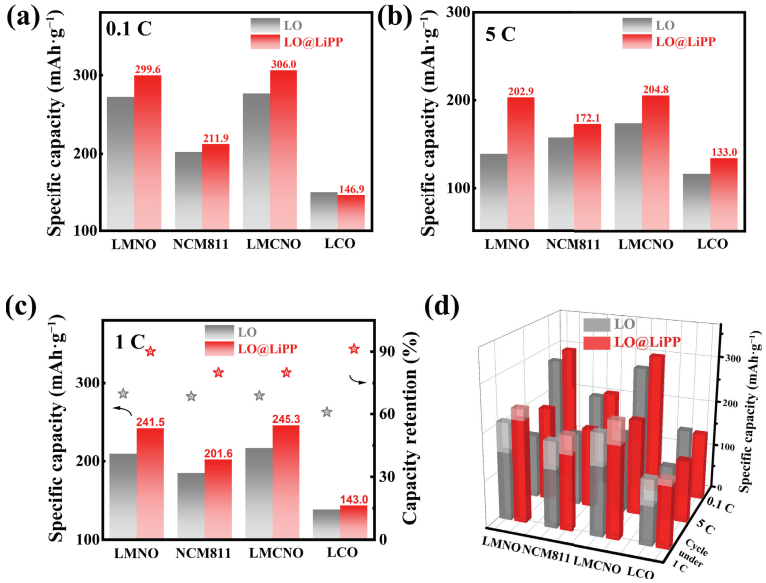

Figure 6 The discharge capacities of cathode materials in this work under (a) 0.1 C and (b) 5 C. (c) The discharge capacities of cathode materials at 1 C (NCM811 at 0.5 C) and the capacity retentions (represented by stars) after 150 cycles. (d) The overall electrochemical performances of LO cathode materials in this work. The patterns with lighter color represent for the discharge capacity decay after 150 cycles.

Table 2 The overall electrochemical performances of cathode materials in this work

	0.1 C capacity (mAh·g^{-1})	1 C capacity (mAh·g^{-1})	1 C capacity and retention after 150 cycles (mAh·g^{-1})	5 C capacity (mAh·g^{-1})
LMNO	272.1	208.9	145.7 (69.7%)	138.7
LMNO@S-LiPP	299.6	241.5	217.6 (90.1%)	202.9
NCM811	201.9	184.4	125.7 (68.4%)[a]	157.4
NCM811@LiPP	211.9	201.6	161.3 (80.0%)[a]	172.1
LMCNO	276.5	216.5	148.5 (68.7%)	173.0
LMCNO@LiPP	306.0	245.3	196.2 (80.0%)	204.8
LCO	150.5	138.0	83.8 (60.9%)	115.2
LCO@LiPP	146.9	143.0	130.6 (91.3%)	133.0

[a]The cycling performance of NCM811 was tested under the current density of 0.5 C.

high-rate performance and long lifespan, which are among the best of all the reported LMNO-based cathode materials. An extremely high capacity of 202.5 mAh·g^{-1} at 1 A·g^{-1} (5 C) is attained with a capacity retention of 85.3% after 300 cycles. Hence, the proposed strategy is expected to offer Co-free Li-rich and other similar LO cathode materials a simple yet effective approach for low-cost electric vehicle battery with high energy density, long lifespan, and rapid charging ability.

Acknowledgements

The authors gratefully acknowledge the financial support from the Ministry of Science and Technology of China (MoST, No. 52090034) and the Higher Education Discipline Innovation Project (No. B12015).

Electronic Supplementary Material: Supplementary material (full details including the synthesis methods, materials characterizations, electrochemical measurements, *ex-situ* tests and sample preparation, additional figures, tables, and notes) is available in the online version of this article at https://doi.org/10.1007/s12274-022-5333-z.

References

[1] Li, M.; Lu, J.; Chen, Z. W.; Amine, K. 30 years of lithium-ion batteries. *Adv. Mater.* **2018**, *30*, 1800561.

[2] Murdock, B. E.; Toghill, K. E.; Tapia-Ruiz, N. A perspective on the sustainability of cathode materials used in lithium-ion batteries. *Adv. Energy Mater.* **2021**, *11*, 2102028.

[3] Huang, A. M.; Ma, Y. C.; Peng, J.; Li, L. L.; Chou, S. L.; Ramakrishna, S.; Peng, S. J. Tailoring the structure of silicon-based materials for lithium-ion batteries via electrospinning technology. *eScience* **2021**, *1*, 141–162.

[4] Wu, M. M.; Zhao, Y.; Zhang, H. T.; Zhu, J.; Ma, Y. F.; Li, C. X.; Zhang, Y. M.; Chen, Y. S. A 2D covalent organic framework with ultra-large interlayer distance as high-rate anode material for lithium-ion batteries. *Nano Res.* **2022**, *15*, 9779–9784.

[5] Wang, J.; He, X.; Paillard, E.; Laszczynski, N.; Li, J.; Passerini, S. Lithium- and manganese-rich oxide cathode materials for high-energy lithium ion batteries. *Adv. Energy Mater.* **2016**, *6*, 1600906.

[6] Zheng, J. M.; Myeong, S.; Cho, W.; Yan, P. F.; Xiao, J.; Wang, C. M.; Cho, J.; Zhang, J. G. Li- and Mn-rich cathode materials: Challenges to commercialization. *Adv. Energy Mater.* **2017**, *7*, 1601284.

[7] He, W.; Guo, W. B.; Wu, H. L.; Lin, L.; Liu, Q.; Han, X.; Xie, Q. S.; Liu, P. F.; Zheng, H. F.; Wang, L. S. et al. Challenges and recent advances in high capacity Li-rich cathode materials for high energy density lithium-ion batteries. *Adv. Mater.* **2021**, *33*, 2005937.

[8] Assat, G.; Tarascon, J. M. Fundamental understanding and practical challenges of anionic redox activity in Li-ion batteries. *Nat. Energy* **2018**, *3*, 373–386.

[9] Zuo, W. H.; Luo, M. Z.; Liu, X. S.; Wu, J.; Liu, H. D.; Li, J.; Winter, M.; Fu, R. Q.; Yang, W. L.; Yang, Y. Li-rich cathodes for rechargeable Li-based batteries: Reaction mechanisms and advanced characterization techniques. *Energy Environ. Sci.* **2020**, *13*, 4450–4497.

[10] Zhang, H. L.; Liu, H.; Piper, L. F. J.; Whittingham, M. S.; Zhou, G. W. Oxygen loss in layered oxide cathodes for Li-ion batteries: Mechanisms, effects, and mitigation. *Chem. Rev.* **2022**, *122*, 5641–5681.

[11] Eum, D.; Kim, B.; Kim, S. J.; Park, H.; Wu, J. P.; Cho, S. P.; Yoon, G.; Lee, M. H.; Jung, S. K.; Yang, W. L. et al. Voltage decay and redox asymmetry mitigation by reversible cation migration in lithium-rich layered oxide electrodes. *Nat. Mater.* **2020**, *19*, 419–427.

[12] Zheng, J. M.; Shi, W.; Gu, M.; Xiao, J.; Zuo, P. J.; Wang, C. M.; Zhang, J. G. Electrochemical kinetics and performance of layered composite cathode material $Li[Li_{0.2}Ni_{0.2}Mn_{0.6}]O_2$. *J. Electrochem. Soc.* **2013**, *160*, A2212.

[13] Yu, X. Q.; Lyu, Y.; Gu, L.; Wu, H. M.; Bak, S. M.; Zhou, Y. N.; Amine, K.; Ehrlich, S. N.; Li, H.; Nam, K. W. et al. Understanding the rate capability of high-energy-density Li-rich layered $Li_{1.2}Ni_{0.15}Co_{0.1}Mn_{0.55}O_2$ cathode materials. *Adv. Energy Mater.* **2014**, *4*, 1300950.

[14] Zhao, H.; Lam, W. Y. A.; Sheng, L.; Wang, L.; Bai, P.; Yang, Y.; Ren, D. S.; Xu, H.; He, X. M. Cobalt-free cathode materials: Families and their prospects. *Adv. Energy Mater.* **2022**, *12*, 2103894.

[15] Zhang, X. F.; Belharouak, I.; Li, L.; Lei, Y.; Elam, J. W.; Nie, A. M.; Chen, X. Q.; Yassar, R. S.; Axelbaum, R. L. Structural and electrochemical study of Al_2O_3 and TiO_2 coated $Li_{1.2}Ni_{0.13}Mn_{0.54}Co_{0.13}O_2$ cathode material using ALD. *Adv. Energy Mater.* **2013**, *3*, 1299–1307.

[16] Liu, H. D.; Qian, D. N.; Verde, M. G.; Zhang, M. H.; Baggetto, L.; An, K.; Chen, Y.; Carroll, K. J.; Lau, D.; Chi, M. F. et al. Understanding the role of NH_4F and Al_2O_3 surface co-modification on lithium-excess layered oxide $Li_{1.2}Ni_{0.2}Mn_{0.6}O_2$. *ACS Appl. Mater. Interfaces* **2015**, *7*, 19189–19200.

[17] Zhang, C. X.; Feng, Y. Z.; Wei, B.; Liang, C. P.; Zhou, L. J.; Ivey, D. G.; Wang, P.; Wei, W. F. Heteroepitaxial oxygen-buffering interface enables a highly stable cobalt-free Li-rich layered oxide cathode. *Nano Energy* **2020**, *75*, 104995.

[18] Zheng, J. M.; Gu, M.; Xiao, J.; Polzin, B. J.; Yan, P. F.; Chen, X. L.; Wang, C. M.; Zhang, J. G. Functioning mechanism of AlF_3 coating on the Li- and Mn-rich cathode materials. *Chem. Mater.* **2014**, *26*, 6320–6327.

[19] Zhu, W.; Tai, Z. G.; Shu, C. Y.; Chong, S. K.; Guo, S. W.; Ji, L. J.; Chen, Y. Z.; Liu, Y. N. The superior electrochemical performance of a Li-rich layered cathode material with Li-rich spinel $Li_4Mn_5O_{12}$ and MgF_2 double surface modifications. *J. Mater. Chem. A* **2020**, *8*, 7991–8001.

[20] Zhao, H.; Li, W. T.; Li, J. X.; Xu, H. Y.; Zhang, C.; Li, J.; Han, C.; Li, Z. L.; Chu, M.; Qiu, X. P. Enhance performances of Co-free Li-rich cathode by eutesctic melting salt treatment. *Nano Energy* **2022**, *92*, 106760.

[21] Ma, Y. T.; Liu, P. F.; Xie, Q. S.; Zhang, G. B.; Zheng, H. F.; Cai, Y. X.; Li, Z.; Wang, L. S.; Zhu, Z. Z.; Mai, L. Q. et al. Double-shell Li-rich layered oxide hollow microspheres with sandwich-like carbon@spinel@layered@spinel@carbon shells as high-rate lithium ion battery cathode. *Nano Energy* **2019**, *59*, 184–196.

[22] Si, M. T.; Wang, D. D.; Zhao, R.; Pan, D.; Zhang, C.; Yu, C. Y.; Lu, X.; Zhao, H. L.; Bai, Y. Local electric-field-driven fast Li diffusion kinetics at the piezoelectric $LiTaO_3$ modified Li-rich cathode-electrolyte interphase. *Adv. Sci.* **2020**, *7*, 1902538.

[23] Zhao, E. Y.; Liu, X. F.; Hu, Z. B.; Sun, L. M.; Xiao, X. L. Facile synthesis and enhanced electrochemical performances of Li_2TiO_3-coated lithium-rich layered $Li_{1.13}Ni_{0.30}Mn_{0.57}O_2$ cathode materials for lithium-ion batteries. *J. Power Sources* **2015**, *294*, 141–149.

[24] Lee, Y.; Lee, J.; Lee, K. Y.; Mun, J.; Lee, J. K.; Choi, W. Facile formation of a Li_3PO_4 coating layer during the synthesis of a lithium-rich layered oxide for high-capacity lithium-ion batteries. *J. Power Sources* **2016**, *315*, 284–293.

[25] Guo, W. B.; Zhang, C. Y.; Zhang, Y. G.; Lin, L.; He, W.; Xie, Q. S.; Sa, B.; Wang, L. S.; Peng, D. L. A universal strategy toward the precise regulation of initial coulombic efficiency of Li-rich Mn-based cathode materials. *Adv. Mater.* **2021**, *33*, 2103173.

[26] Zhu, X. H.; Meng, F. Q.; Zhang, Q. H.; Xue, L.; Zhu, H.; Lan, S.; Liu, Q.; Zhao, J.; Zhuang, Y. H.; Guo, Q. B. et al. $LiMnO_2$ cathode stabilized by interfacial orbital ordering for sustainable lithium-ion batteries. *Nat. Sustain.* **2021**, *4*, 392–401.

[27] Liu, J. X.; Wang, J. Q.; Ni, Y. X.; Zhang, Y. D.; Luo, J.; Cheng, F. Y.; Chen, J. Spinel/lithium-rich manganese oxide hybrid nanofibers as cathode materials for rechargeable lithium-ion batteries. *Small Methods* **2019**, *3*, 1900350.

[28] Liu, P. F.; Zhang, H.; He, W.; Xiong, T. F.; Cheng, Y.; Xie, Q. S.; Ma, Y. T.; Zheng, H. F.; Wang, L. S.; Zhu, Z. Z. et al. Lithium deficiencies engineering in Li-rich layered oxide $Li_{1.098}Mn_{0.533}Ni_{0.113}Co_{0.138}O_2$ for high-stability cathode. *J. Am. Chem. Soc.* **2019**, *141*, 10876–10882.

[29] Zhang, X. D.; Shi, J. L.; Liang, J. Y.; Yin, Y. X.; Zhang, J. N.; Yu, X. Q.; Guo, Y. G. Suppressing surface lattice oxygen release of Li-rich cathode materials via heterostructured spinel $Li_4Mn_5O_{12}$ coating. *Adv. Mater.* **2018**, *30*, 1801751.

[30] Zhu, Y. F.; Xiao, Y.; Dou, S. X.; Kang, Y. M.; Chou, S. L. Spinel/post-spinel engineering on layered oxide cathodes for sodium-ion batteries. *eScience* **2021**, *1*, 13–27.

[31] Zhu, A. P.; Wu, J. H.; Wang, B. Y.; Zhou, J. W.; Zhang, Y.; Guo, Y.; Wu, K. P.; Wu, H.; Wang, Q.; Zhang, Y. Harmonious dual-riveting interface induced from niobium oxides coating toward superior stability of Li-rich Mn-based cathode. *ACS Appl. Mater. Interfaces* **2021**, *13*, 61248–61257.

[32] Li, Q. Y.; Zhou, D.; Zhang, L. J.; Ning, D.; Chen, Z. H.; Xu, Z. J.; Gao, R.; Liu, X. Z.; Xie, D. H.; Schumacher, G. et al. Tuning anionic redox activity and reversibility for a high-capacity Li-rich Mn-based oxide cathode via an integrated strategy. *Adv. Funct. Mater.* **2019**, *29*, 1806706.

[33] Xiao, Y. H.; Miara, L. J.; Wang, Y.; Ceder, G. Computational screening of cathode coatings for solid-state batteries. *Joule* **2019**, *3*, 1252–1275.

[34] Du, Y. H.; Sheng, H.; Meng, X. H.; Zhang, X. D.; Zou, Y. G.; Liang, J. Y.; Fan, M.; Wang, F. Y.; Tang, J. L.; Cao, F. F. et al. Chemically converting residual lithium to a composite coating layer to enhance the rate capability and stability of single-crystalline Ni-rich cathodes. *Nano Energy* **2022**, *94*, 106901.

[35] Xu, L. Q.; Sun, Z. H.; Zhu, Y.; Han, Y.; Wu, M. M.; Ma, Y. F.; Huang, Y.; Zhang, H. T.; Chen, Y. S. A Li-rich layered-spinel cathode material for high capacity and high rate lithium-ion batteries fabricated via a gas-solid reaction. *Sci. China Mater.* **2020**, *63*, 2435–2442.

[36] Sun, Z. H.; Xu, L. Q.; Dong, C. Q.; Zhang, H. T.; Zhang, M. T.; Ma, Y. F.; Liu, Y. Y.; Li, Z. J.; Zhou, Y.; Han, Y. et al. A facile gaseous sulfur treatment strategy for Li-rich and Ni-rich cathode materials with high cycling and rate performance. *Nano Energy* **2019**, *63*, 103887.

[37] Meng, J. X.; Xu, L. S.; Ma, Q. X.; Yang, M. Q.; Fang, Y. Z.; Wan, G. Y.; Li, R. H.; Yuan, J. J.; Zhang, X. K.; Yu, H. J. et al. Modulating crystal and interfacial properties by W-gradient doping for highly stable and long life Li-rich layered cathodes. *Adv. Funct. Mater.* **2022**, *32*, 2113013.

[38] Zheng, H. F.; Zhang, C. Y.; Zhang, Y. G.; Lin, L.; Liu, P. F.; Wang, L. S.; Wei, Q. L.; Lin, J.; Sa, B.; Xie, Q. S. et al. Manipulating the local electronic structure in Li-rich layered cathode towards superior electrochemical performance. *Adv. Funct. Mater.* **2021**, *31*, 2100783.

[39] Luo, D.; Ding, X. K.; Hao, X. D.; Xie, H. X.; Cui, J. X.; Liu, P. Z.; Yang, X. H.; Zhang, Z. H.; Guo, J. J.; Sun, S. H. et al. Ni/Mn and Al dual concentration-gradients to mitigate voltage decay and capacity fading of Li-rich layered cathodes. *ACS Energy Lett.* **2021**, *6*, 2755–2764.

[40] Cai, Y. X.; Ku, L.; Wang, L. S.; Ma, Y. T.; Zheng, H. F.; Xu, W. J.; Han, J. T.; Qu, B. H.; Chen, Y. Z.; Xie, Q. S. et al. Engineering oxygen vacancies in hierarchically Li-rich layered oxide porous microspheres for high-rate lithium ion battery cathode. *Sci. China Mater.* **2019**, *62*, 1374–1384.

[41] Lee, M. J.; Lho, E.; Oh, P.; Son, Y.; Cho, J. Simultaneous surface modification method for $0.4Li_2MnO_3$-$0.6LiNi_{1/3}Co_{1/3}Mn_{1/3}O_2$ cathode material for lithium ion batteries:Acid treatment and $LiCoPO_4$ coating. *Nano Res.* **2017**, *10*, 4210–4220.

[42] Peng, J. M.; Li, Y.; Chen, Z. Q.; Liang, G. M.; Hu, S. J.; Zhou, T. F.; Zheng, F. H.; Pan, Q. C.; Wang, H. Q.; Li, Q. Y. et al. Phase

compatible $NiFe_2O_4$ coating tunes oxygen redox in Li-rich layered oxide. *ACS Nano* **2021**, *15*, 11607–11618.
[43] Sun, J. M.; Sheng, C. C.; Cao, X.; Wang, P. F.; He, P.; Yang, H. J.; Chang, Z.; Yue, X. Y.; Zhou, H. S. Restraining oxygen release and suppressing structure distortion in single-crystal Li-rich layered cathode materials. *Adv. Funct. Mater.* **2022**, *32*, 2110295.
[44] Zhang, X. D.; Shi, J. L.; Liang, J. Y.; Yin, Y. X.; Guo, Y. G.; Wan, L. J. Structurally modulated Li-rich cathode materials through cooperative cation doping and anion hybridization. *Sci. China Chem.* **2017**, *60*, 1554–1560.
[45] Ruther, R. E.; Callender, A. F.; Zhou, H.; Martha, S. K.; Nanda, J. Raman microscopy of lithium-manganese-rich transition metal oxide cathodes. *J. Electrochem. Soc.* **2015**, *162*, A98.
[46] Lanz, P.; Villevieille, C.; Novák, P. *Ex situ* and *in situ* Raman microscopic investigation of the differences between stoichiometric $LiMO_2$ and high-energy $xLi_2MnO_3\cdot(1-x)LiMO_2$ (M = Ni, Co, Mn). *Electrochim. Acta* **2014**, *130*, 212.
[47] Huang, W. W.; Frech, R. *In situ* Raman spectroscopic studies of electrochemical intercalation in $Li_xMn_2O_4$-based cathodes. *J. Power Sources* **1999**, *81–82*, 616–620.
[48] Ding, X. K.; Luo, D.; Cui, J. X.; Xie, H. X.; Ren, Q. Q.; Lin, Z. An ultra-long-life lithium-rich $Li_{1.2}Mn_{0.6}Ni_{0.2}O_2$ cathode by three-in-one surface modification for lithium-ion batteries. *Angew. Chem., Int. Ed.* **2020**, *59*, 7778–7782.
[49] Johnson, C. S.; Li, N.; Lefief, C.; Vaughey, J. T.; M. Thackeray, M. Synthesis, characterization and electrochemistry of lithium battery electrodes: $xLi_2MnO_3\cdot(1-x)LiMn_{0.333}Ni_{0.333}Co_{0.333}O_2$ ($0 \le x \le 0.7$). *Chem. Mater.* **2008**, *20*, 6095–6106.
[50] Li, Q. Y.; Ning, D.; Zhou, D.; An, K.; Schuck, G.; Wong, D.; Kong, W. J.; Schulz, C.; Schumacher, G.; Liu, X. F. Tuning both anionic and cationic redox chemistry of Li-Rich $Li_{1.2}Mn_{0.6}Ni_{0.2}O_2$ via a "Three-in-One" Strategy. *Chem. Mater.* **2020**, *32*, 9404–9414.
[51] Chen, Q.; Pei, Y.; Chen, H. W.; Song, Y.; Zhen, L.; Xu, C. Y.; Xiao, P. H.; Henkelman, G. Highly reversible oxygen redox in layered compounds enabled by surface polyanions. *Nat. Commun.* **2020**, *11*, 3411.
[52] Vu, N. H.; Im, J. C.; Unithrattil, S.; Im, W. B. Synergic coating and doping effects of Ti-modified integrated layered-spinel $Li_{1.2}Mn_{0.75}Ni_{0.25}O_{2+\delta}$ as a high capacity and long lifetime cathode material for Li-ion batteries. *J. Mater. Chem. A* **2018**, *6*, 2200–2211.
[53] Li, L.; Wang, L. C.; Zhang, X. X.; Xue, Q.; Wei, L.; Wu, F.; Chen, R. J. 3D reticular $Li_{1.2}Ni_{0.2}Mn_{0.6}O_2$ cathode material for lithium-ion batteries. *ACS Appl. Mater. Interfaces* **2017**, *9*, 1516–1523.
[54] Hua, W. B.; Wu, Z. G.; Chen, M. Z.; Knapp, M.; Guo, X. D.; Indris, S.; Binder, J. R.; Bramnik, N. N.; Zhong, B. H.; Guo, H. P. et al. Shape-controlled synthesis of hierarchically layered lithium transition-metal oxide cathode materials by shear exfoliation in continuous stirred-tank reactors. *J. Mater. Chem. A* **2017**, *5*, 25391–25400.
[55] Zhao, T. L.; Li, L.; Chen, R. J.; Wu, H. M.; Zhang, X. X.; Chen, S.; Xie, M.; Wu, F.; Lu, J.; Amine, K. Design of surface protective layer of LiF/FeF_3 nanoparticles in Li-rich cathode for high-capacity Li-ion batteries. *Nano Energy* **2015**, *15*, 164–176.
[56] Liu, Y. C.; Wang, J.; Wu, J. W.; Ding, Z. Y.; Yao, P. H.; Zhang, S. L.; Chen, Y. A. 3D cube-maze-like Li-rich layered cathodes assembled from 2D porous nanosheets for enhanced cycle stability and rate capability of lithium-ion batteries. *Adv. Energy Mater.* **2020**, *10*, 1903139.
[57] Yang, X. R.; Wang, C. W.; Yan, P. F.; Jiao, T. P.; Hao, J. L.; Jiang, Y. Y.; Ren, F. C.; Zhang, W. G.; Zheng, J. M.; Cheng, Y. et al. Pushing lithium cobalt oxides to 4.7 V by lattice-matched interfacial engineering. *Adv. Energy Mater.* **2022**, *12*, 2200197.
[58] Wang, E. R.; Xiao, D. D.; Wu, T. H.; Liu, X. S.; Zhou, Y. N.; Wang, B. Y.; Lin, T.; Zhang, X.; Yu, H. J. Al/Ti synergistic doping enhanced cycle stability of Li-rich layered oxides. *Adv. Funct. Mater.* **2022**, *32*, 2201744.
[59] Zhu, Z.; Gao, R.; Waluyo, I.; Dong, Y. H.; Hunt, A.; Lee, J.; Li, J. Stabilized Co-free Li-rich oxide cathode particles with an artificial surface prereconstruction. *Adv. Energy Mater.* **2020**, *10*, 2001120.
[60] Zhang, J. C.; Zhang, Q. H.; Wong, D.; Zhang, N.; Ren, G. X.; Gu, L.; Schulz, C.; He, L. H.; Yu, Y.; Liu, X. F. Addressing voltage decay in Li-rich cathodes by broadening the gap between metallic and anionic bands. *Nat. Commun.* **2021**, *12*, 3071.
[61] Wang, Y.; Wang, Z. X.; Wu, D. X.; Niu, Q. H.; Lu, P. S.; Ma, T. H.; Su, Y. B.; Chen, L. Q.; Li, H.; Wu, F. Stable Ni-rich layered oxide cathode for sulfide-based all-solid-state lithium battery. *eScience* **2022**, *2*, 537–545.
[62] Han, J. G.; Lee, J. B.; Cha, A.; Lee, T. K.; Cho, W.; Chae, S.; Kang, S. J.; Kwak, S. K.; Cho, J.; Hong, S. Y. et al. Unsymmetrical fluorinated malonatoborate as an amphoteric additive for high-energy-density lithium-ion batteries. *Energy Environ. Sci.* **2018**, *11*, 1552–1562.
[63] Mu, P. Z.; Zhang, H. R.; Jiang, H. Z.; Dong, T. T.; Zhang, S.; Wang, C.; Li, J. D.; Ma, Y.; Dong, S. M.; Cui, G. L. Bioinspired antiaging binder additive addressing the challenge of chemical degradation of electrolyte at cathode/electrolyte interphase. *J. Am. Chem. Soc.* **2021**, *143*, 18041–18051.
[64] Andersson, A. M.; Abraham, D. P.; Haasch, R.; MacLaren, S.; Liu, J.; Amine, K. Surface characterization of electrodes from high power lithium-ion batteries. *J. Electrochem. Soc.* **2002**, *149*, A1358.
[65] Zhang, F. L.; Zhou, X. A.; Fu, X. L.; Wang, C.; Wang, B.; Liang, W. B.; Wang, P.; Huang, J.; Li, S. Y. Which is the winner between the single-crystalline and polycrystalline $LiNi_{0.80}Co_{0.15}Al_{0.05}O_2$ cathode in the lithium-ion battery? *Mater. Today Energy* **2021**, *22*, 100873.
[66] Wu, S. X.; Yang, Y. J.; Liu, C. B.; Liu, T. F.; Zhang, Y. P.; Zhang, B. K.; Luo, D.; Pan, F.; Lin, Z. *In-situ* polymerized binder: A three-in-one design strategy for all-integrated SiO_x anode with high mass loading in lithium ion batteries. *ACS Energy Lett.* **2021**, *6*, 290–297.
[67] Aurbach, D.; Zaban, A.; Ein-Eli, Y.; Weissman, I.; Chusid, O.; Markovsky, B.; Levi, M.; Levi, E.; Schechter, A.; Granot, E. Recent studies on the correlation between surface chemistry, morphology, three-dimensional structures and performance of Li and Li-C intercalation anodes in several important electrolyte systems. *J. Power Sources* **1997**, *68*, 91–98.
[68] Kawamura, T.; Okada, S.; Yamaki, J. I. Decomposition reaction of $LiPF_6$-based electrolytes for lithium ion cells. *J. Power Sources* **2006**, *156*, 547–554.
[69] Jo, C. H.; Cho, D. H.; Noh, H. J.; Yashiro, H.; Sun, Y. K.; Myung, S. T. An effective method to reduce residual lithium compounds on Ni-rich $Li[Ni_{0.6}Co_{0.2}Mn_{0.2}]O_2$ active material using a phosphoric acid derived Li_3PO_4 nanolayer. *Nano Res.* **2015**, *8*, 1464–1479.
[70] Luo, D.; Cui, J. X.; Zhang, B. K.; Fan, J. M.; Liu, P. Z.; Ding, X. K.; Xie, H. X.; Zhang, Z. H.; Guo, J. J.; Pan, F. et al. Ti-based surface integrated layer and bulk doping for stable voltage and long life of Li-rich layered cathodes. *Adv. Funct. Mater.* **2021**, *31*, 2009310.
[71] Li, Q. Y.; Ning, D.; Zhou, D.; An, K.; Wong, D.; Zhang, L. J.; Chen, Z. H.; Schuck, G.; Schulz, C.; Xu, Z. J. et al. The effect of oxygen vacancy and spinel phase integration on both anionic and cationic redox in Li-rich cathode materials. *J. Mater. Chem. A* **2020**, *8*, 7733–7745.
[72] Bao, L. Y.; Wei, L.; Fu, N. T.; Dong, J. Y.; Chen, L.; Su, Y. F.; Li, N.; Lu, Y.; Li, Y. J.; Chen, S. et al. Urea-assisted mixed gas treatment on Li-rich layered oxide with enhanced electrochemical performance. *J. Energy Chem.* **2022**, *66*, 123–132.
[73] Yang, J. C.; Chen, Y. X.; Li, Y. J.; Xi, X. M.; Zheng, J. C.; Zhu, Y. L.; Xiong, Y. K.; Liu, S. W. Encouraging voltage stability upon long cycling of Li-rich Mn-based cathode materials by Ta-Mo dual doping. *ACS Appl. Mater. Interfaces* **2021**, *13*, 25981–25992.
[74] Yu, R. Z.; Wang, X. Y.; Fu, Y. Q.; Wang, L. W.; Cai, S. Y.; Liu, M. H.; Lu, B.; Wang, G.; Wang, D.; Ren, Q. F. et al. Effect of magnesium doping on properties of lithium-rich layered oxide cathodes based on a one-step co-precipitation strategy. *J. Mater. Chem. A* **2016**, *4*, 4941–4951.
[75] Ni, L. S.; Guo, R. T.; Fang, S. S.; Chen, J.; Gao, J. Q.; Mei, Y.; Zhang, S.; Deng, W. T.; Zou, G. Q.; Hou, H. S. et al. Crack-free single-crystalline Co-free Ni-rich $LiNi_{0.95}Mn_{0.05}O_2$ layered cathode. *eScience* **2022**, *2*, 116–124.